Magneto-optical garnets for integrated optoelectronic devices

T. Wehlus*, T. Körner, S. Leitenmeier, A. Heinrich, and B. Stritzker

Institute of Physics, University of Augsburg, 86135 Augsburg, Germany

Received 5 May 2010, revised 5 November 2010, accepted 8 November 2010
Published online 8 December 2010

Keywords bismuth iron garnet, Faraday rotation, magnetooptics

* Corresponding author: e-mail thomas.wehlus@physik.uni-augsburg.de, Phone: +49 821 598 3498, Fax: +49 821 598 3425

One of the efforts of integrated optics is the integration of macroscopic optical components such as an optical isolator on a single chip. Therefore magneto-optically active materials with high Faraday rotations are needed. Bismuth iron garnet (BIG) $Bi_3Fe_5O_{12}$ is known for its high Faraday rotation at room temperature, but it forms in a non-thermodynamic way and only grows on garnet substrates like gadolinium gallium garnet (GGG) $Gd_3Ga_5O_{12}$. Our ambition was to investigate the possibility of depositing such an integrated optical device based on magneto-optical BIG. A general overview of our extensive fundamental research is given in this paper. We first analysed the growth mechanisms of BIG on GGG, especially the nucleation process and the film growth which are important for BIG film synthesis. Then we worked on a garnet buffer system to enable film formation on other substrate materials like silicon or fused silica. To obtain the optical constants of the deposited material, a fitting algorithm was implemented. It calculates the optical properties of material stacks from transmission measurements. Furthermore, we wanted to vary the lattice constants of the garnets for a better adaption to the substrates. Because different rare earth elements have different atomic radii, it should be possible to vary the lattice constant by incorporating these atoms in the crystal. Therefore a number of rare earth doped garnets were produced and their film properties were analysed. During the buffer development we found an oscillatory effect in the Faraday rotation, which was examined in detail.

1 Introduction In the year 1845 M. Faraday reported that certain materials affect polarised electro-magnetic waves when exposed to an external magnetic field by turning the angle of polarisation [1]. The direction and the amount of this rotation depend only on the direction and the grade of the magnetisation, but not on the propagation direction of the transmitted light. This nonlinear optical effect was named Faraday effect and the effected rotation angle is called Faraday rotation θ.

$$\theta(\omega) = V(\omega)Hd \tag{1}$$

Equation (1) states the Faraday effect and gives the Faraday rotation as a function of the external magnetic field H, the sample thickness d and a matter-dependent Verdet constant $V(\omega)$. It is a function of the wavelength ω, and hence the Faraday rotation is also.

A possible way to utilise Faraday's magneto-optical (MO) effect is to construct a device known as an optical isolator [2]. Optical isolators are one-way streets for light and they can act as unidirectional restrictor valves in optical communication networks. Placed on both sides of an optical amplifier, they filter out backscattered light from the signal line and for this reason increase the amplifier efficiency.

Figure 1 depicts a schematic diagram of an optical isolator. Three parts form such a device. Two polarisers placed around a magnetised MO active material, which could be an MO garnet crystal for example. Polariser 1 at the entrance is rotated $+45^\circ$ against polariser 2 at the isolator exit. Thus light going through the optical isolator is linearly polarised by polariser 1 and enters the MO garnet. The garnet is set to rotate the light polarisation by $+45^\circ$, thus it is aligned parallel to polariser 2 afterwards and can pass easily. But incident, e.g. reflected, light from the opposite side will pass polariser 2 first and will then be rotated within the garnet by $+45^\circ$ also. Thus finally its polarisation direction is perpendicular to polariser 1. So consequently light from the opposite side cannot pass the optical isolator.

To build integrated optical isolators, materials capable of high Faraday rotation are needed. The garnet materials classify as one of these [3, 4].

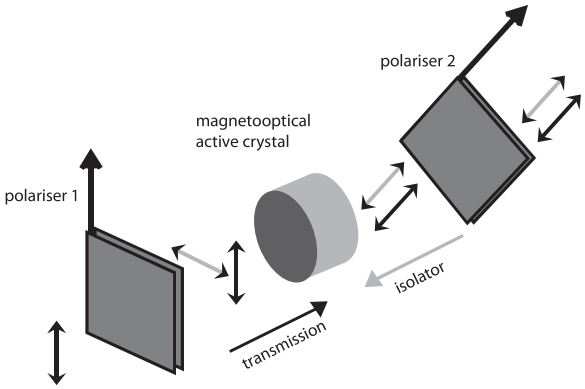

Figure 1 A schematic diagram of an optical isolator.

Yttrium iron garnet (YIG) $Y_3Fe_5O_{12}$ for example shows high Faraday rotation and low optical losses in the near-infrared spectral range, and therefore YIG is widely used in MO devices [5]. In 1969 Buhrer discovered that a substitution of yttrium by bismuth significantly increases the Faraday rotation [6]. This was further analysed by Hansen et al. [7–9]. A theoretical approach to the Faraday rotation in bismuth iron garnet (BIG) is given in Refs. [10–15].

Due to the difference between the bismuth and yttrium ion radii, a fully substituted BIG $Bi_3Fe_5O_{12}$ is not thermodynamically stable [16]. The use of liquid phase epitaxy, normally used for growing garnets like YIG, is thus not applicable for BIG [17]. It is necessary to use non-equilibrium processes such as reactive ion beam sputtering or pulsed laser deposition (PLD) for their synthesis [18]. As already shown by Kahl et al. PLD is a good method to create thin BIG films on, for example gadolinium gallium garnet (GGG) $Gd_3Ga_5O_{12}$ single crystal substrates [19, 20, 40]. The high Faraday rotation of BIG of more than 20°/μm at a wavelength of 532 nm makes it the ideal material for the miniaturisation of macroscopic MO devices.

The first step in our work was to investigate the nucleation process and optimise the epitaxial film growth of BIG and YIG films by PLD onto GGG single-crystal substrates. To reveal the growth mechanism and characterise the deposited film material and the film to substrate interface, we utilised techniques like transmission electron microscopy (TEM), environmental scanning electron microscopy (ESEM), energy dispersive X-ray analysis (EDX), atomic force microscopy (AFM), Rutherford backscattering spectroscopy (RBS) and X-ray diffraction (XRD). Also a special Faraday rotation measurement setup (FRMS) was designed. To determine the optical constants of the films, a simulation with a fitting algorithm was implemented.

The ability to grow YIG and BIG films onto GGG substrates is one asset to the realisation of an integrated MO component, where more substrate materials than solely GGG are eligible for the integration of electrical and optical components on a single chip. That is why, in a second step, we investigated and developed garnet buffer systems to enable BIG film deposition on other substrate materials like silicon, silica or fused silica.

Furthermore, we introduced a number of rare earth dopants into YIG and studied their influence on the resulting garnet film properties. In the centre of our focus was the effect of the dopant on the garnet lattice constant.

We found an oscillation of the Faraday rotation with the wavelength in some of our samples and could explain this effect by the occurrence of birefringence in the affected silica substrates as a result of mechanical strain due to the ongrown film.

2 Target preparation and characterisation The general approach to synthesise a PLD target for BIG deposition is the mixing, pressing and sintering of oxide powders, e.g. Bi_2O_3 and Fe_2O_3, as described in Lux et al. [21]. Beacuse the mixing of the starting materials is a mechanical process, the distribution of the powder particles in the product is not uniform. This leads to stoichiometrically inhomogeneous targets and thus causes problems during the formation of the desired BIG phase in the ablation process.

To prepare dense homogeneous targets, Nassar et al. [22] suggested the use of a sol–gel process instead. We adapted this process to our material system and improved it further. The process flowchart is given in Fig. 2. We start by dissolving metallic salts into an aqueous solution, mixed with HNO_3 and glucose. The resulting solution is heated up to a temperature of 100 °C under constant stirring. In the solution, the glucose acts as a sequestrant.

After a while the sol alters and becomes transparent. It is then slowly dehydrated until the desired gel forms, in which the educts are now distributed homogeneously. In the next

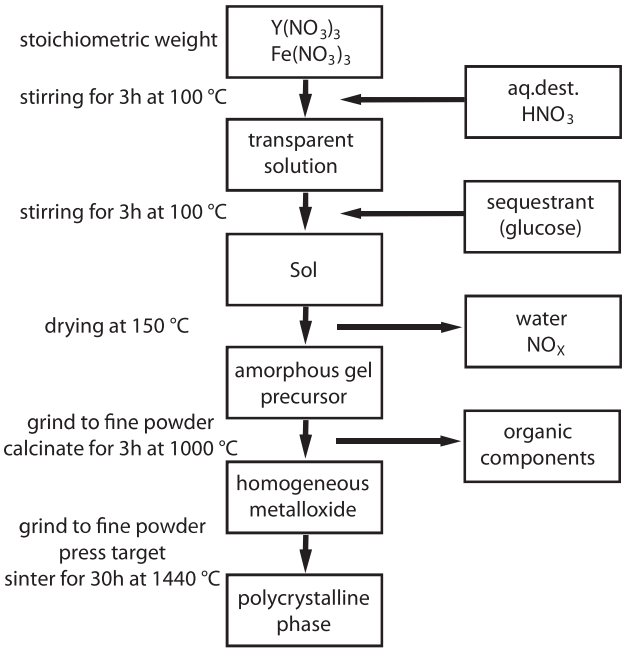

Figure 2 The flowchart of sol–gel process for target preparation [36]. The example is based on a YIG target.

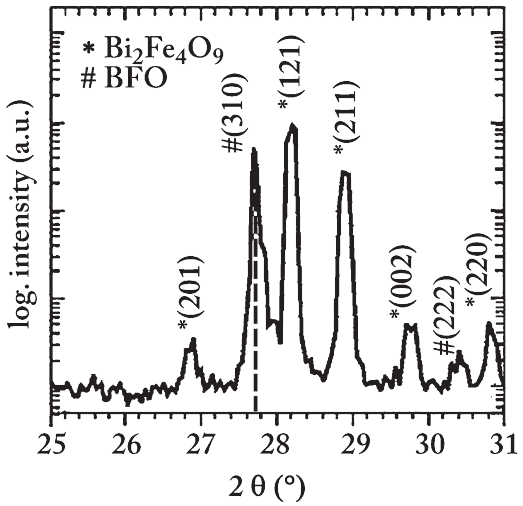

Figure 3 The XRD characteristic spectrum for the BIG precursor targets. The indexed peaks designated with * refer to the $Bi_2Fe_4O_9$ phase, # corresponds to $Bi_{25}FeO_{40}$ (BFO).

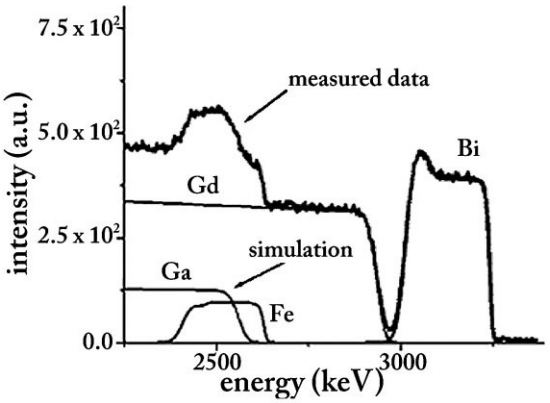

Figure 4 The RBS spectrum of a BIG film on GGG. The measured data with the model fit are shown.

step, water is removed from the gel in a drying cabinet. The remaining powder is calcined to remove organic components, pressed into a cylindrical form and sintered at an appropriate temperature for 30 h. In the targets for the deposition of thermodynamically stable garnets, the corresponding garnet phase forms during the final sintering step and can be verified by its associated reflections in a XRD scan. More details are given in Refs. [23, 24].

As mentioned above, no garnet phase forms for BIG during the target preparation due to thermodynamic reasons. But in the XRD spectrum we find reflections originating from two other crystalline oxides in the target, $Bi_2Fe_4O_9$ and $Bi_{25}FeO_{40}$ (BFO). An exemplary XRD spectrum obtained from a BIG precursor target is shown in Fig. 3. The bismuth to iron ratio of a BIG film is $c_{Bi}/c_{Fe} = 0.60$. Compared to that $Bi_2Fe_4O_9$ is a bismuth-deficient phase with a c_{Bi}/c_{Fe} ratio of only 0.50. On the other hand BFO is a phase with an iron deficiency ($c_{Bi}/c_{Fe} = 0.04$). The composition proportion can be changed by the stoichiometry of the target ingredients. For a BIG target it exactly meets the ratio necessary for a $c_{Bi}/c_{Fe} = 0.60$ over the whole target.

3 BIG film deposition For the deposition of the BIG films discussed in this paper, a standard PLD setup was used [36]. An overview for PLD is precisely discussed in Refs. [25–29]. A KrF excimer laser (Lambda Physik LPX 300) generates UV laser pulses ($\lambda = 248$ nm, 30 ns). The laser beam passes a lens and a rectangular shaped aperture to compensate for beam divergence and to blend out the inhomogeneous rim of the beam. A second lens in front of the deposition chamber scales down the aperture and focuses the beam on the target. The target itself is located inside a vacuum deposition chamber, which the beam enters through a view port. The energy density on the target reaches up to 5 J/cm^2 (at 1.0 J/pulse).

Prior to the start of the BIG film deposition the target surface was sandpapered and a pre-ablation of 20000 laser pulses set place. The cylindrically shaped target rotates during the ablation process. The high laser pulse energy density on the target causes emission of the target material. A plasma plume forms, which is directed perpendicularly to the target surface. The substrate holder is placed within the plume range about 5 cm away from the target on a resistive heater.

The atmosphere in the deposition chamber is controlled by admitting a defined flow of process gas while constantly pumping the chamber. During the ablation process, the oxygen pressure p_{O_2}, the laser pulse energy E_L and the temperature in the sample holder T_H were measured. Previous to the ablation process, the substrates were cleaned in an ultrasonic bath of first acetone and second isopropyl alcohol, rinsed with pure water and then dried under Nitrogen gas flow.

It is most important to obtain the desired thin-film stoichiometry during deposition. Therefore the composition and structure of the deposited BIG films were measured by RBS. A typical RBS spectrum for a BIG film on GGG is shown in Fig. 4. It confirms the correct stoichiometry of the film after the ablation and thus the correct target composition. It is also possible to determine the film thickness from the RBS measurement.

4 BIG film growth on GGG

4.1 Influence of the deposition parameters on the BIG film quality Deposition parameters have a large influence on the properties of the growing film [27]. Counted among them are the substrate temperature T, laser pulse energy E, laser pulse rate f_L and the composition and pressure of the atmosphere during film growth. We examined the influence of the oxygen pressure p_O during the PLD on the stoichiometry of the deposited film. While p_O was varied from 4.0×10^{-3} to 7.0×10^{-2} mbar, the other parameters were set to $T = 550\,^{\circ}$C, $E = 1.0$ J, 72000 pulses and $f_L = 20$ Hz. It was found that the Bi/Fe ratio c_{Bi}/c_{Fe} increases with oxygen pressure, as shown in Table 1. Samples

Table 1 The Bi/Fe ratio increases with oxygen pressure.

p_O (mbar)	c_{Bi}/c_{Fe}	p_O (mbar)	c_{Bi}/c_{Fe}
4.0×10^{-3}	0.43	3.0×10^{-2}	0.57
6.0×10^{-3}	0.44	5.0×10^{-2}	0.80
1.0×10^{-2}	0.67	7.0×10^{-2}	0.96
2.0×10^{-2}	0.66		

deposited at pressures in the range of $(1.0–3.0) \times 10^{-2}$ mbar are closest to the BIG stoichiometric value of the Bi/Fe ratio ($c_{Bi}/c_{Fe} = 0.60$).

We also investigated the influence of different deposition temperatures $T = 400–650\,^{\circ}C$ on the BIG film growth and film stoichiometry. The other deposition parameters were set to $p_{O_2} = 1.0 \times 10^{-2}$ mbar, $E = 0.8$ J, 60000 pulses and $f_L = 10$ Hz. Epitaxial BIG growth was found in a temperature range from $T = (500–600)\,^{\circ}C$. The XRD showed the best crystallinity for 550 °C as depicted in Fig. 5.

In Fig. 5 a strong BIG (004) reflection is clearly visible. Also the GGG (004) reflex of the GGG substrate can be observed. Although not present in the shown pattern, the expected position of the (310) peak of the BFO phase has been marked. It becomes visible for the non-optimal deposition temperatures under 530 °C. An influence of the lasers frequency f_L or the pulse energy E on the film quality could not be found, but the growth rate of course climbs with a higher laser energy.

4.2 Initial BIG film growth We used (001) and (111) GGG substrates to study the BIG growth. The BIG films were deposited using optimised deposition parameters ($T_1 = 550\,^{\circ}C$, $p_{O_2} = 1.0 \times 10^{-2}$ mbar, $E = 0.8$ J and $f_L = 10$ Hz) as described above. During the ablation process the *in situ* reflection high-energy electron diffraction (RHEED) patterns were taken to monitor the formation of the BIG film. RHEED is a very surface-sensitive analytical method [32]. The used RHEED system operates at an electron energy from 10 to 50 keV with an incident beam angle of 0.1–5.0°. Due to a differential pumping system in the electron gun, the RHEED system can be operated at chamber pressures up to 1.0×10^{-2} mbar. This is a sufficiently high pressure for BIG film deposition.

In Fig. 6 two *in situ* RHEED patterns recorded during BIG film deposition are shown. The analysis of the recorded patterns clearly indicates that BIG grows epitaxially on different GGG crystal cuts. The diffraction patterns can be explained as cuts through a three-dimensional reciprocal lattice, so the dominant growth mechanism is island growth. Because of these findings, we expect uniformly oriented growth islands on the film surface. Their shape should be characteristic for the crystallographic orientation of the substrate. To verify this, a series of AFM and ESEM pictures were taken. For this work a Fei XL30 ESEM FEG was used. It utilises a field emission electron source and can be operated at electron energies up to 30 keV. Besides the ESEM mode, it

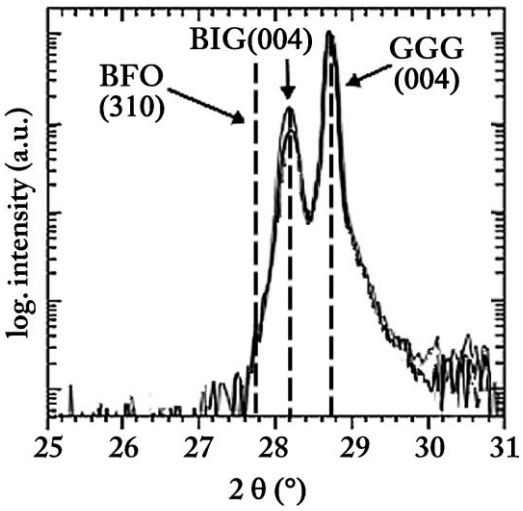

Figure 5 The XRD spectrum of two BIG films at $T_1 = 550\,^{\circ}C$ and $T_2 = 600\,^{\circ}C$. The theoretical positions of the BFO (310), BIG (004) and GGG (004) peaks are marked.

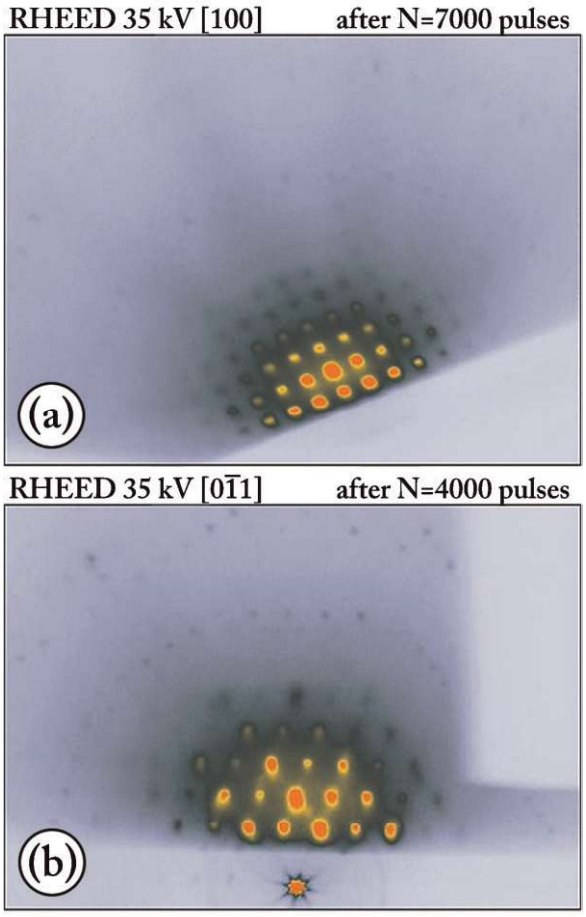

Figure 6 (online color at: www.pss-a.com) The RHEED diffraction patterns of BIG films growing on GGG. (a) GGG (001) along the [100] direction after 7000 pulses. (b) GGG (111) along the [0$\bar{1}$1] direction after 4000 pulses [30, 31].

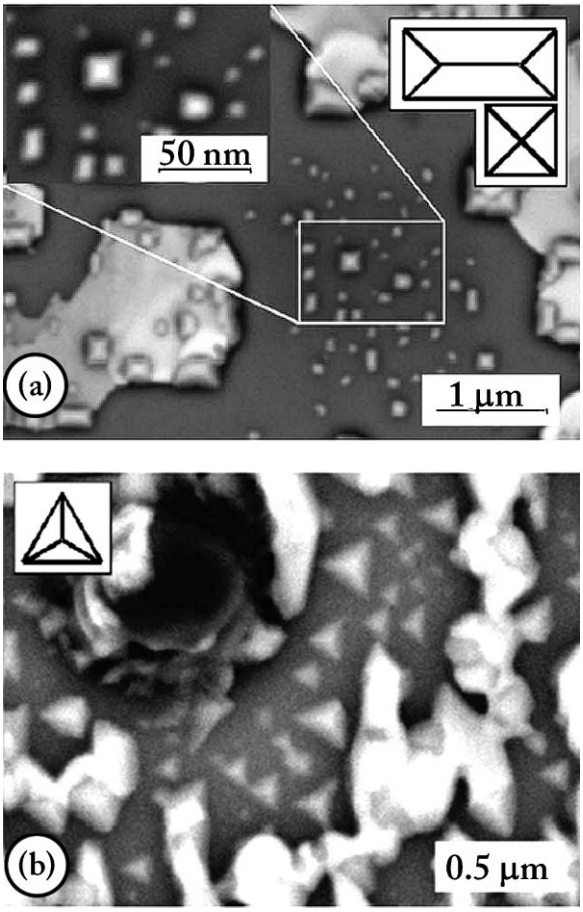

Figure 7 ESEM BSE images of BIG growth island structures on different GGG cuts. (a) The rectangular shaped islands on the GGG (001) substrate. (b) On the GGG (111) substrate triangular structures are found. Both images are taken at a background pressure of $p_{H_2O} = 27$ Pa and a beam energy $E = 8$ kV [21].

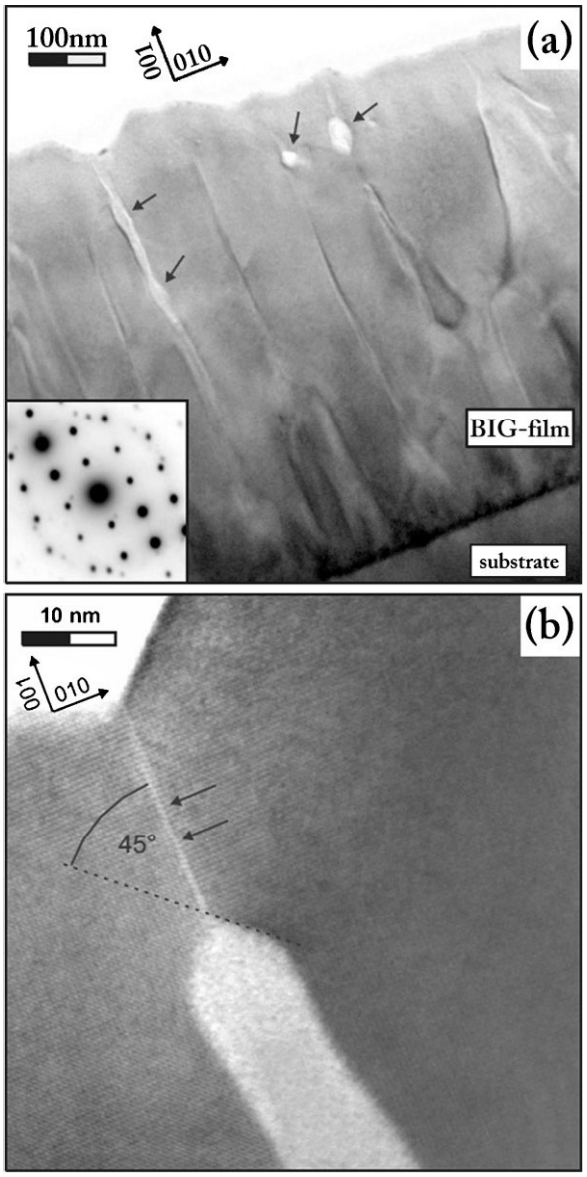

Figure 8 A TEM cross-section bright field image taken at $U = 300$ kV. (a) A general overview over the sample. Defects in the film are marked with arrows. The inset shows the corresponding diffraction pattern. Additional spots indicate the presence of non-garnet crystalline impurity phases. (b) A high resolution image of an inclusion between two crystal grains. It is overgrown at an angle of 45°. The grain boundary reaches up to the film surface [31].

can be operated in a normal high-vacuum mode also. The signal of various electron detectors, e.g. back-scattered electrons (BSE) or secondary electrons, can be used for the picture generation. The materials analysis is possible with an attached EDX system.

In Fig. 7 ESEM images in BSE contrast of the BIG thin films grown on (001) and (111) GGG are shown. The images were taken at a beam energy of $E = 8$ kV and a background water pressure of $p_{H_2O} = 27$ Pa. It is clearly visible that BIG adapts to the crystal lattice of GGG, forming small islands on the substrate surface. The shape of the islands corresponds to the position of the unit cell relative to the surface. Rectangular shaped islands grow on GGG (001) substrates (Fig. 7a), while triangular shaped structures are found on GGG (111) substrates (Fig. 7b). Further on in the process these islands or grains grow until they get into contact with each other. They then form a closed BIG film for which epitaxial growth was confirmed by XRD pole figure measurements.

To further investigate the BIG film, cross-section TEM images were taken. For this work a Philips CM30 and a Philips CM300 TEM were used. Both microscopes are working at an acceleration voltage $U = 300$ kV. For a cross-section sample preparation, one sample is sawn in two halves and then glued together film to film. Using a mechanical thinning system, the centre of this package is reduced to a thickness of 10 µm. Afterwards a further thinning with a 5 keV argon ion beam is performed.

In Fig. 8a, a bright field cross-section TEM image of a BIG film on the GGG substrate is shown. The small grains

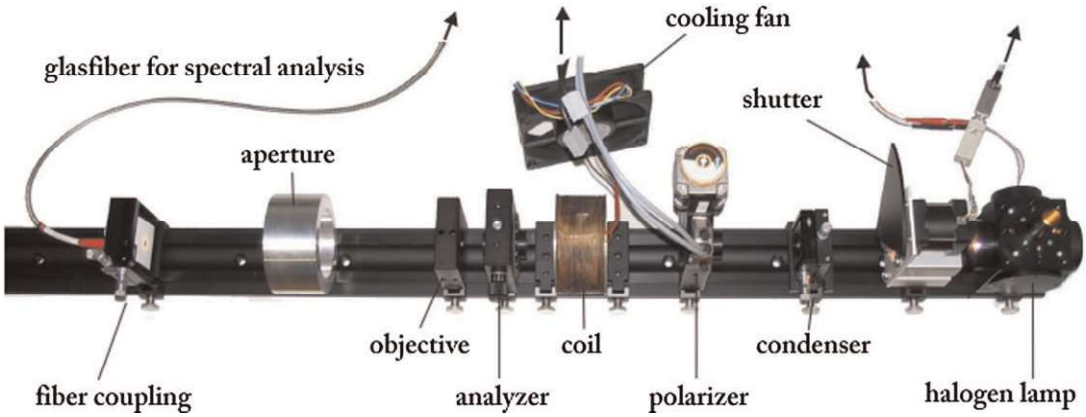

Figure 9 (online color at: www.pss-a.com) The Faraday rotation measurement setup. From right to left: halogen lamp (light source), shutter, condenser lens, Glan–Thompson prism as the polariser, field coil, Glan–Thompson prism as the analyser, objective lens to focus the light trough the aperture on the fibre coupling.

that had formed on the surface, as seen in Fig. 7, are overgrown by each other. Thus the structure directly on the surface has a high degree of disorder, which resolves after the first 100 nm of film thickness. Then wider pillars with a width of approximately 100 nm have formed, reaching up to the film surface. Embedded between these pillars are inclusions and defects (marked with arrows). A diffraction pattern of the crystal lattice shows additional reflexes. These indicate errors in the BIG crystal lattice (Fig. 8).

In Fig. 8b, a larger area of an inclusion between two crystal grains is shown. The inclusion is overgrown by the BIG at an angle of 45° with the so formed grain boundary reaching up to the surface. The surface of the BIG films was investigated by AFM scans, and an example is shown in Fig. 10. The scan shows a maximum surface level difference of 80 nm and a RMS surface roughness of 14 nm. This corresponds well with the TEM observations (Fig. 8a). More details can be found in Refs. [30, 31].

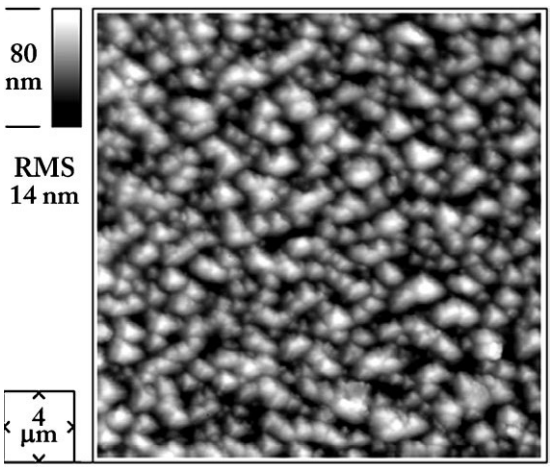

Figure 10 AFM image of BIG film surface on GGG (111) substrate. The roughness is $R_q = 14$ nm. The analysed area is $4 \times 4\ \mu m^2$ [30].

5 Faraday rotation measurement setup To measure the Faraday rotation, a special setup (FRMS) was built (Fig. 9). The basic function of the FRMS is easy to understand. White light from a halogen lamp is linearly polarised by a Glan–Thompson prism and then sent through the magnetised sample. Afterwards it goes through another Glan–Thompson prism working as analyser and is then coupled via an optical fibre into a spectrometer. Various lenses form and guide the beam of light through the setup. The measurement itself is completely automatised and controlled by software. The coil shown in Fig. 9 can be replaced by a permanent magnet setup with $B = 150$ mT. The light source is also computer controlled and the intensity is adjusted prior to each measurement to get maximum sensitivity from the spectrometer. The polariser is turned in 5° steps, and on each step a preset number of spectra is summed up. After a 180° turn, the magnetisation is reversed and the measurement is repeated. Thus we ensure that we really have Faraday rotation and no other effects, like for example tension induced birefringence. After the measurement the data is analysed by solving the Jones matrices and performing a Fourier analysis of the data. Thus it is possible to calculate the Faraday rotation θ. For a detailed description of the calculations, see Ref. [30].

In Fig. 11 typical Faraday rotation spectra are shown. The Faraday rotation increases linearly with the film thickness d whereas the transmission $T(\lambda)$ weakens. For this reason some of the curves do not reach the left frame of the graph. There is not enough intensity left to measure. With the FRMS it is also possible to measure the spectral transmission of the film. From these transmission data, it is possible to calculate the optical constants of the inspected film.

6 Transmittance spectra simulation of BIG In this section, we want to demonstrate how we gain the film thickness d, the refractive index n and the extinction coefficient k from the measured transmission spectra $T(\lambda)$. As an example, a bilayer of BIG/YIG on SiO_2 was measured,

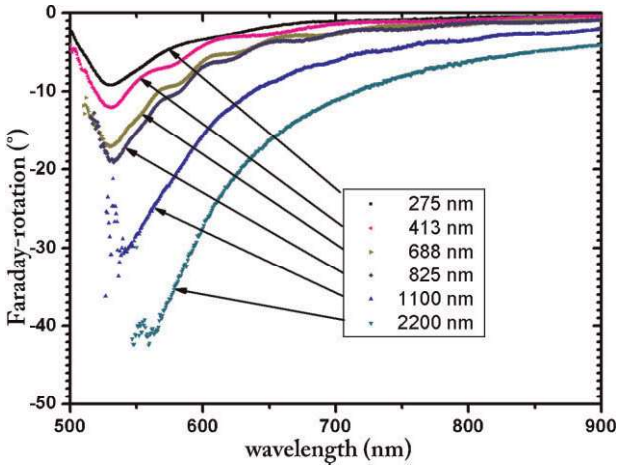

Figure 11 (online color at: www.pss-a.com) Faraday rotation spectra of BIG films of thicknesses from 275 to 2200 nm. $B = 150$ mT.

and the parameters mentioned above were determined by a fitting algorithm. To deduce this algorithm, we adapted the formalism of Yeh [33] leading to Eq. (2).

$$T(\lambda) = \frac{n_s}{n_0}\left|\frac{1}{M_{11}}\right|^2 \frac{1}{1-(1-T_{S\to A})(1-T_{S\to L})}$$
$$\text{with } M = D_0^{-1}\prod_{l=-1}^{m}\underbrace{D_1 P_1 D_1^{-1}}_{\text{layer 1}} D_s\,. \tag{2}$$

In Eq. (2), $T(\lambda)$ is the transmission, $T_{S\to A}$ is the transmittance from the substrate into the air and $T_{S\to L}$ is the transmittance from the substrate into the next layer.

$$T_{S\to A} = \frac{n_0}{n_s}\left|\frac{1}{(D_s^{-1}D_0)_{11}}\right|$$
$$\text{and} \tag{3}$$
$$T_{S\to L} = \frac{n_m}{n_s}\left|\frac{1}{(D_s^{-1}D_m)_{11}}\right|.$$

In Eq. (2) the matrix M includes the transfer matrix D_1 and the propagation matrix for layer 1 P_1. These are given in Eq. (4).

$$P_1 = \begin{pmatrix} \exp[in_1(2\pi/\lambda)d_1)] & 0 \\ 0 & \exp[-in_1(2\pi/\lambda)d_1)] \end{pmatrix}$$
$$D_1 = \begin{pmatrix} 1 & 1 \\ n_1 & -n_1 \end{pmatrix} \tag{4}$$

Homogeneity has great influence on the optical transmittance spectrum of thin films. So if the model does not consider the surface roughness, the determined extinction coefficients, film thicknesses and refractive indices are incorrect. AFM measurements show that film thicknesses roughly follow a Gaussian distribution. Because of that we extended the model to consider a standardised normally distributed film thickness.

$$T_R(\lambda, \sigma_d, d, n, k, s) = \frac{1}{\sigma_d\sqrt{2\pi}}\int_{-\infty}^{\infty}\exp\left(-\frac{1}{2}\left(\frac{d'-d}{\sigma_d}\right)^2\right)T(\lambda, d', n, k, s)\,\mathrm{d}d'. \tag{5}$$

In Eq. (5), λ represents the wavelength, d is the mean value and σ_d is the standard deviation of the film thickness. In our model, σ_d is used as a measure of the film surface roughness. Using this model, we were able to simulate the transmittance spectra of BIG/YIG on a SiO_2 layer. The fit is shown in Fig. 12a. Because n and k are spectral, the appropriate models were chosen [20]. For the calculation of the refractive indices of BIG and YIG we used:

$$n = A + \left(\frac{B^2}{\lambda}\right) \tag{6}$$

For the extinction coefficient of YIG:

$$k(\lambda)_{YIG} = \frac{\lambda}{4\pi}\frac{a}{(\lambda-b)^{1,8}+c} \tag{7}$$

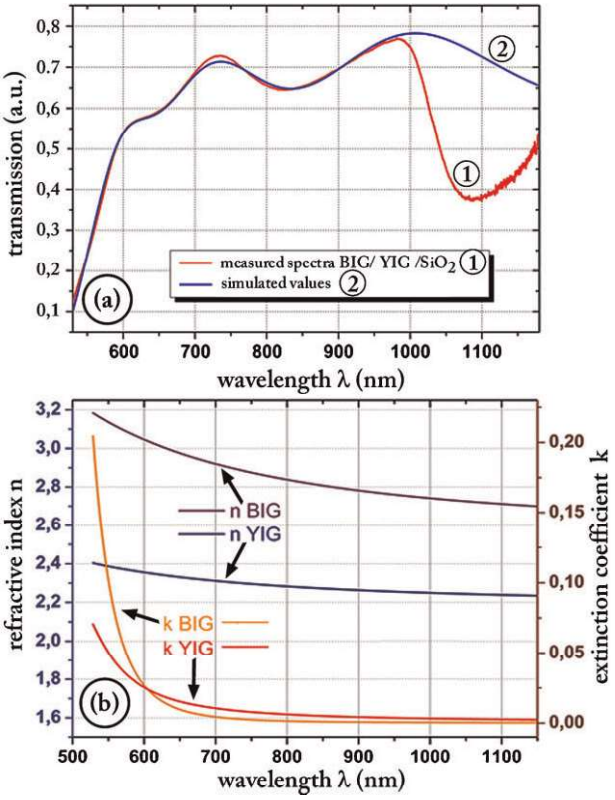

Figure 12 (online color at: www.pss-a.com) (a) The measured and simulated transmission spectra of a BIG/YIG stack on SiO_2. The spectra do not fit for wavelengths above $\lambda = 1.0$ μm because of model simplifications. The fitting area is set from 550 to 950 nm. (b) The calculated n and k spectra for BIG and YIG.

Table 2 The comparison of the layer thicknesses measured by RBS and determined by simulation.

substrate	measured by RBS		calculated	
	YIG (nm)	BIG (nm)	YIG (nm)	BIG (nm)
SiO_2 1010	177	625	148	605
SiO_2 1120	17	350	20	354
SiO_2 0001	14	523	16	555
SiO_2 0001	104	490	112	462

and for BIG:

$$k(\lambda)_{\mathrm{BIG}} = \frac{\lambda}{4\pi} \exp\left[\left(\frac{a}{\lambda}\right)^2 - b\right] \tag{8}$$

was assumed.

The results for n and k of the YIG and BIG films are shown in Fig. 12b. The simulated thicknesses d were compared to the values determined by RBS measurements. The difference between the thickness determination by the RBS measurement and the simulation is lower than 10%. A comparison of the results is given in Table 2. So the determination of the film thicknesses and the optical parameters can be done successfully by fitting a transmittance spectrum. More details are given in Koerner et al. [34].

7 Buffer systems To deposit BIG on a non-garnet substrate like silicon or fused silica, a method of forming a thin garnet buffer layer had to be found. The idea was to choose a thermodynamically stable garnet like YIG. Therefore we fabricated a YIG target by the sol–gel method described above. After the sol–gel process, the target was dried at 150 °C, then calcined at 1000 °C for 3 h, pressed into a cylindrical shape and sintered at 1400 °C for 30 h. The RBS and XRD analysis revealed the correct stoichiometry and a clear YIG phase.

For the film deposition we used silicon, an amorphous fused silica substrate and various cuts of silica. After an optimisation process similar that of BIG all ablations were done at $T = 700\,^{\circ}\mathrm{C}$, $E = 2.0\,\mathrm{J/cm^2}$, $p_{O_2} = 3.0 \times 10^2\,\mathrm{mbar}$ and $f_L = 10\,\mathrm{Hz}$. After PLD, the YIG buffers were annealed at 1050 °C under oxygen atmosphere for 3 h. This lead to the formation of a sole polycrystalline YIG phase. A powder XRD pattern of an annealed YIG film is given in Fig. 13.

Following the annealing process we used ESEM and AFM to investigate the film surface morphology. We found a surface pervaded by cracks. An image of a YIG buffered BIG film on SiO_2 (001) is shown in Fig. 14. The area between the cracks had the expected roughness morphology of BIG.

The problem results from the different thermal expansion coefficients of the garnet materials ($\mathrm{YIG} = 10.0 \times 10^{-6}(1/K)$) and fused silica ($\mathrm{SiO_2} = 0.59 \times 10^{-6}(1/K)$). This leads to cracks during the cooling phase of the annealing process. Even a strongly reduced cooling rate could not prevent the crack formation. Further measurements showed

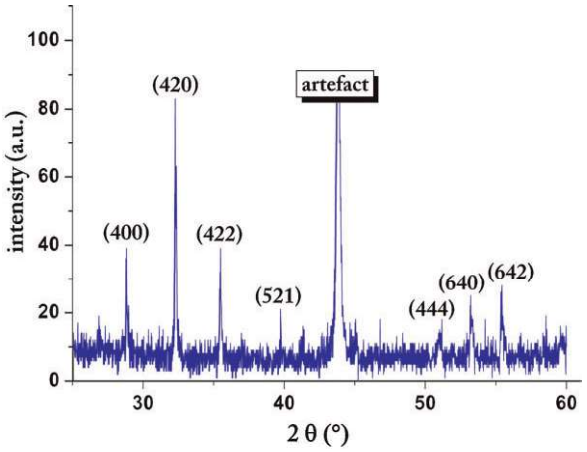

Figure 13 (online color at: www.pss-a.com) The powder XRD pattern of a YIG-sample annealed at 1050 °C. Strong reflections are marked and the corresponding lattice planes are given.

that the cracks in the YIG buffer are partly overgrown by BIG during the BIG ablation process. BIG grown on a polycrystalline YIG buffer shows the same Faraday rotation as one grown on GGG substrates.

In Fig. 15, a cross-section TEM image of a YIG buffered BIG film on amorphous SiO_2 is shown. The interface between the YIG and the BIG layers is clearly visible. Here we observed that the periodical structure of the YIG buffer is transferred to the BIG layer. The small image in the middle visualises the tension in the substrate. The films have shrunk during the cooling phase of the annealing process and thus are generating cracks in the films down and into the substrate. It was also possible to integrate YIG buffered systems on various other materials like silicon and Al_2O_3. In summary one can say that the most important thing for a buffer formation is the ability of the substrate to withstand the high temperatures during the annealing process. Further information on buffered garnet systems can be found in Refs. [35, 36].

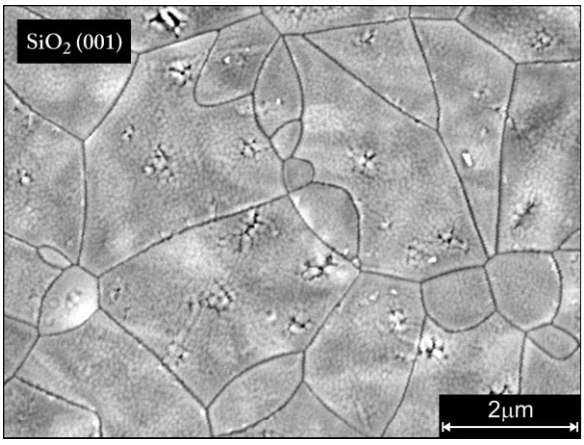

Figure 14 BIG/YIG on SiO_2 (001). The cracks in the film surface are clearly visible.

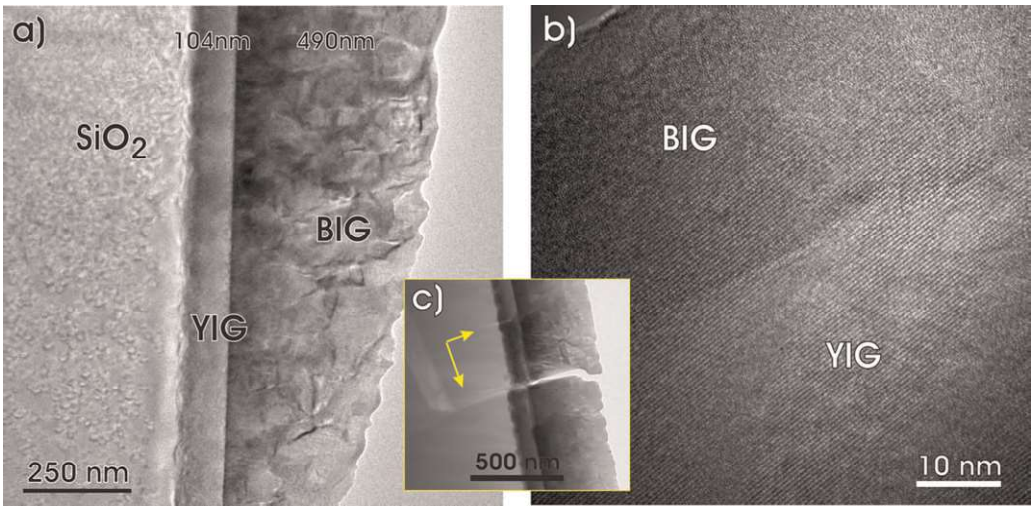

Figure 15 (online color at: www.pss-a.com) A high resolution TEM image of BIG/YIG on amorphous SiO_2 [34]. (a) An overview over the layer system. (b) The interface between the YIG and the BIG layer. The periodical structure of the YIG buffer is transferred to the BIG layer. (c) The tension in the substrate is clearly visible.

8 Rare earth doping of YIG As already mentioned, the radii of the Y^{3+} and Bi^{3+} ions in YIG and BIG differ. This leads to larger lattice constants and therefore to problems in the adaption of BIG to the YIG buffer. Besides bismuth, yttrium can be substituted by many other rare-earth elements. For a lot of possible substituents, e.g. samarium (Sm), europium (Eu), gadolinium (Gd), erbium (Er), thulium (Tm) or lutetium (Lu), the resulting garnet lattice constants are already known because these materials are thermodynamically stable. Thereby Sm^{3+} is the largest possible thermodynamically stable substituent.

We next wanted not only investigate the influence of a full substitution by ions with a radius larger then Sm^{3+}, but also the influence of a partial substitution. Thus, we wanted to analyse the possibilities to create a multilayer stack with a wide range of possible adjustments regarding optical properties like Faraday rotation and the optical constants, or morphological properties like roughness and crack formation. Our focus was on the substitution by neodymium (Nd), praseodymium (Pr), lantanium (La) and cerium (Ce). Additionally, to compare full and partial substitutions by these elements, partial substitutions by bismuth (Bi) were tested. An overview over the lattice constants for a number of films is given in Fig. 16.

In Fig. 17 the influence of a partial substitution of bismuth is shown. The maximum possible Faraday rotation grows with the bismuth content, while the ideal deposition temperature shifts to the left. The effect of the substitution on the Faraday rotation and the lattice constant is proportional to the bismuth content. The Faraday rotation increases from nearly 0°/μm for pure YIG to over 30°/μm for BIG, while the lattice constant increases from 12.42 Å for YIG to 12.62 Å for BIG.

Similar measurements were made for the other materials. An overview of all the results is given in Table 3. In that table, the influence of a substitution of

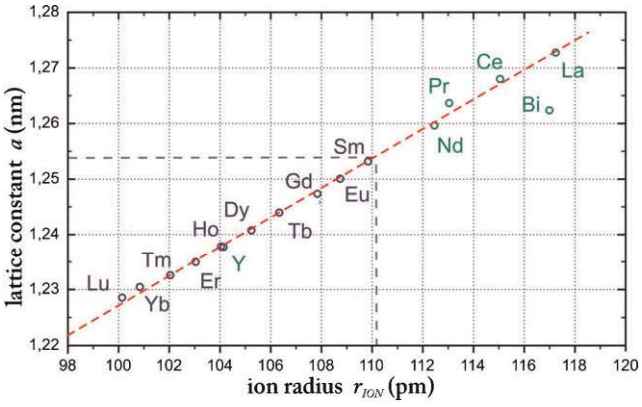

Figure 16 (online color at: www.pss-a.com) The effect of the rare earth ion radius on the lattice parameters of the garnet. The two lines mark the border of the thermodynamically stable area [16].

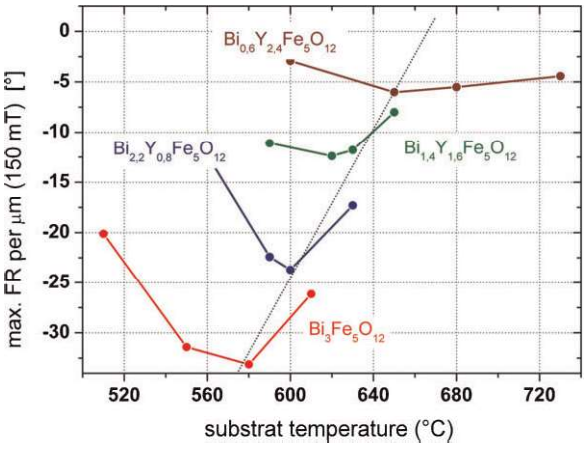

Figure 17 (online color at: www.pss-a.com) The influence of the bismuth substitution of YIG on the Faraday rotation.

Table 3 The influence of a substitution of bismuth by a rare earth element on the Faraday rotation $|\theta_F|$, the maximum of the Faraday rotation $\lambda\theta_F$, the lattice constant $a_{lattice}$ and the ion radius r_{ion}.

$RE_xBi_{3-x}IG$ (x)	$\lvert\theta_F\rvert$ °/μm	$\lambda\theta_F$ (nm)	$a_{lattice}$ (Å)	r_{ion} (pm)
Bi	33	530	12.62 (BIG)	117
Y [0.8...2.4]	24...6	–	12.38 (YIG)	104
Nd [0.1...3]	27...0	–	12.63...12.62	112.3
Pr [0.25...3]	20...3	530...500	12.60...12.71	113
La [0.5...3]	9...0	530...495	12.67...12.86	117.2
CeIG	4	–	12.68	–
Ce [0.1...2.5]	29...0	530...520	12.62	115
Er [0.18...0.6]	21...16	530...525	12.61...12.58	103

The substituent is given in the first row.

bismuth by a rare earth element on various properties, such as the Faraday rotation or the ion radius is given.

9 Faraday rotation oscillations During our investigations on the YIG buffers on various substrates, we found an oscillation in the Faraday rotation. After the annealing step, a 400 nm YIG buffer on SiO_2 $(10\bar{1}0)$ showed a Faraday rotation oscillating with λ between $+0.5$ and $-0.5°$. This is much more than expected for a YIG film of that thickness.

We tested various substrates and found that this effect occurs only on SiO_2 $(10\bar{1}0)$ and $(11\bar{2}0)$ cuts. The problem was, that the measurements could not be reproduced. Every time a substrate was inserted in the sample holder it showed the oscillations, but with a different magnitude. After a while we found that the strength of the oscillation correlates with the tension that the FRMS sample holder applies on the substrate. An example of these measurements is given in Fig. 18. The oscillation in the Faraday rotation increases with the externally applied tension. A definite tension also applies to the curve marked as *no tension*. This is caused by the stress that evolves during the cooling process at the end of the annealing step.

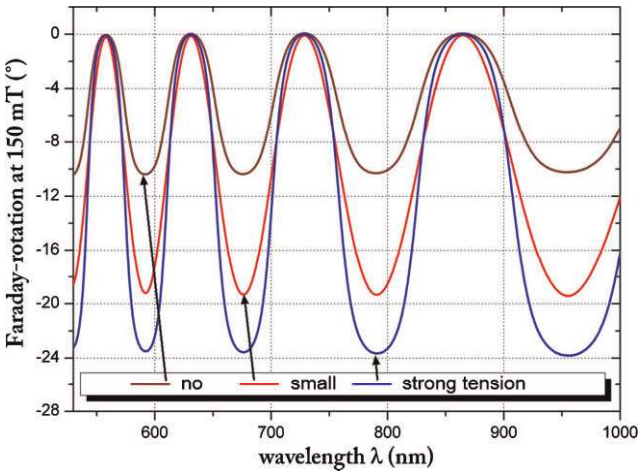

Figure 18 (online color at: www.pss-a.com) The oscillation of the Faraday rotation at various substrate tensions. The oscillations get stronger with higher tensions.

To explain this observation, the effect of a stress-induced birefringence must be used. In our case, crystalline SiO_2 develops an additional stress induced birefringence, which leads to a varied refraction of light with differing chirality [37, 38]. The structure of the crystal plays an important role for birefringence. Because of this it is important that the light enters the crystal along a special axis. The birefringence only appears if light enters perpendicular to the main axis. This prerequisite is fulfilled for SiO_2 with the $(10\bar{1}0)$ and $(11\bar{2}0)$ cuts. A schema of the SiO_2 crystal is given in Fig. 20.

To explain the oscillations in detail, we simulated the optical properties of the material stack. Therefore the stack is divided in layers of differing optical properties. To identify these layers a cross-section TEM image of the material was taken (Fig. 19). The left side of the image gives a description of the used model stack based on the TEM image on the right side. We believe that the source of the birefringence is located in a thin SiO_2 layer next to the interface between the substrate and buffer.

After the deposition of the YIG layer normally an annealing step at 1000 °C is performed. During this step a polycrystalline YIG layer forms and the substrates melts in a transitional area with Y und Fe diffusing into it [39]. After this area the crystalline SiO_2 area follows. In this area the tension applied by the YIG buffer during the cooling phase relaxes. In this partially tensed up area, the stress-induced birefringence is located. The simulation showed that the stress relaxes in a depth up to 1 μm from the surface. This fits to the depth determined by TEM measurements.

By using the stack composition and the film thicknesses the Faraday rotation can be simulated. The results and measurements are shown in Fig. 21. The results of the simulation fit very well to the measured values. The developed model is therefore capable of a consistent explanation of the observed extraordinary effect of the oscillation in the Faraday rotation.

10 Summary and outlook In the present paper we studied the properties of MO garnets with a focus on the application in an integrated MO device based on BIG. A new method for PLD target preparation, especially for garnet targets, was presented. With this method it is feasible to

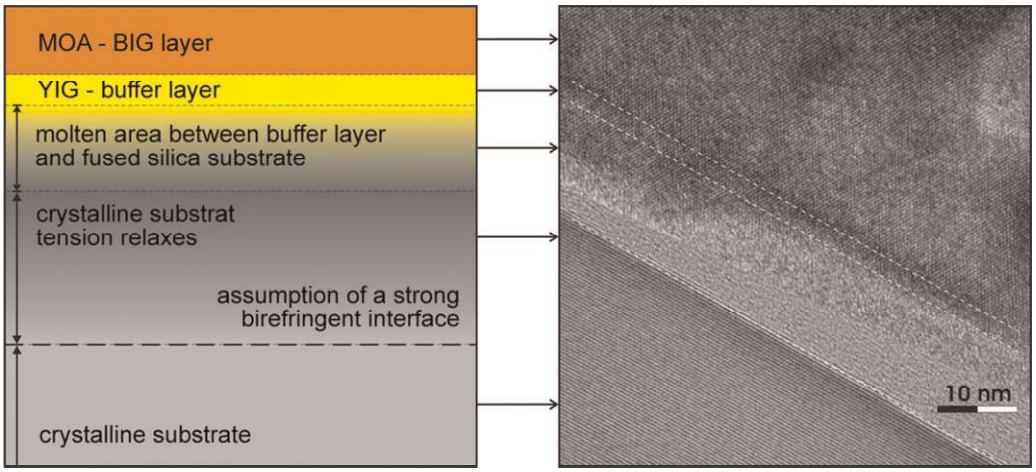

Figure 19 (online color at: www.pss-a.com) Left side: The model developed for the simulation of the YIG buffer systems. A thin YIG layer rests in a transitional area with Y und Fe diffused into it. Right side: The TEM image of a $(10\bar{1}0)$ sample as the base for the model stack. Molten or crystalline areas are marked.

produce dense homogeneous targets and thus enhance the film quality.

They were used to deposit thin films for a detailed analysis of BIG growth parameters. The optimised deposition parameters are $T = 550\,^{\circ}\mathrm{C}$ and $p_{O_2} = 2.0 \times 10^{-2}$ mbar with insignificant influence of the laser pulse energy and repetition rate. Island growth was found for PLD of BIG on GGG substrates. BIG adapts to the structure of the garnet substrate, growing in pillars about 100 nm wide. The interface on the BIG film shows a higher degree of disorder, which dissolves within the first 100 nm. On GGG the film growth is epitaxial, and the film roughness is about $R_q = 14$ nm. We build a setup to measure the Faraday rotation and transmission spectra of our films. From the transmission spectra it was possible to calculate the thickness and determine the optical constants n and k for YIG and BIG.

These values indicate that BIG is a suitable material for integrated optics. For the transfer to non-garnet substrates, a YIG buffer was developed successfully. The formation of this buffer is feasible for any substrate that withstands the necessary 1050 °C annealing process. The optimal YIG deposition conditions are $T = 700\,^{\circ}\mathrm{C}$ and $p_{O_2} = 3.0 \times 10^{2}$ mbar. Annealing should be done under oxygen gas flow for 3 h at 1050 °C. This leads to a polycrystalline YIG buffer. The minimum buffer thickness for BIG growth is about 10 nm after the annealing step. BIG deposited on the buffer exhibits the same Faraday rotation as BIG grown on GGG. It grows with a higher degree of disorder. On SiO_2 and silicon, it shows cracks due to the different thermal expansion coefficients between the substrate and film. The roughness of BIG grown on GGG compared to BIG grown on a buffer is similar.

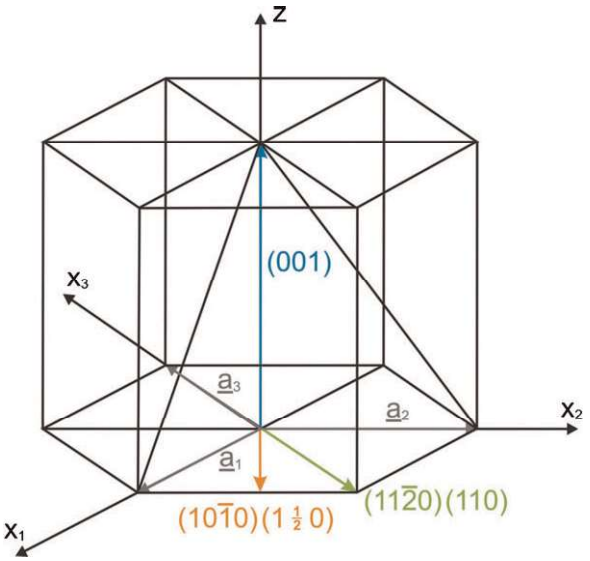

Figure 20 (online color at: www.pss-a.com) The schematice of the crystal axis in a hexagonal lattice. The lattice vectors and the different cuts of the crystal are marked.

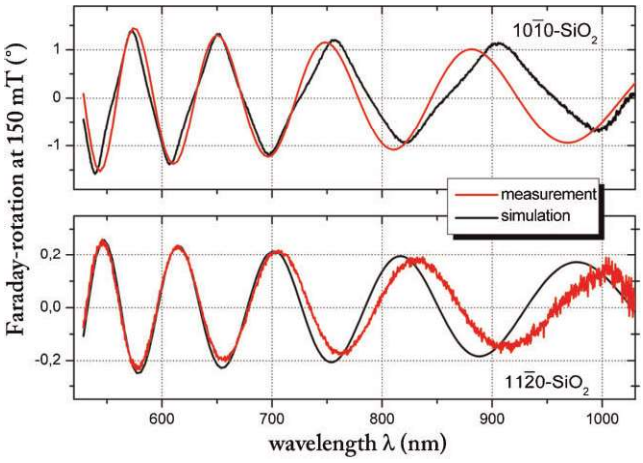

Figure 21 (online color at: www.pss-a.com) The measurement and simulation of the material stack.

For being able to design a useful garnet stack, we tried to optimise the BIG films by doping with rare-earth garnets. We are now able to provide garnets with a wide range of different lattice constants.

While working on the buffer layer an oscillatory effect in the buffer systems was found on some special SiO_2 crystal cuts. A simulation was developed to analyse the source of this rotation. It was found that the effect can be explained by birefringence. The strain originates from thermal stress applied during the cooling process at the end of the annealing step.

Summing up, we showed that it is feasible to create a BIG based thin film MO device on silicon or (fused) silica substrates. The next steps will include investigations of film structuring methods to form a planar waveguide. Due to the chemical stability of the garnet, laser cutting could be a promising method. To reduce reflections inside the waveguide, a further reduction of the film roughness is necessary. This could be done by ion bombardment or plasma etching techniques. The problem of film cracks could be addressed by a variation of the substrate material. A special designed layer stack could lead to stress relaxation in the film and thus to fewer cracks.

Acknowledgements The authors would like to thank the Deutsche Forschungsgemeinschaft (Schwerpunktprogramm 1157) for their financial support of this work.

References

[1] M. Faraday, Phil. Trans. R. Soc. London **136:1**, 20 (1846).
[2] L. J. Aplet and J. W. Carson, Appl. Opt. **3**, 544 (1964).
[3] A. K. Zvezdin and V. A. Kotov, Modern Magnetooptics and Magnetooptical Materials (Institute of Physics Publishing, Bristol, 1997).
[4] A. Heinrich, Magnetooptische Materialien und Megnetooptische Untersuchungen an Supraleitern, Universitaet Augsburg, Habilitationsschrift, 2006.
[5] H. Doetsch, N. Bahlmann, O. Zhuromskyy, M. Hammer, L. Wilkens, R. Gerhardt, and P. Hertel, J. Opt. Soc. **22**, 240 (2005).
[6] C. F. Buhrer, J. Phys. A **40**, 4500 (1969).
[7] P. Hansen, K. Witter, and W. Tolksdorf, Phys. Rev. B **27**, 6608 (1983).
[8] P. Hansen and J.-P. Krumme, Thin Solid Films **114**, 69 (1984).
[9] P. Hansen, W. Tolksdorf, and K. Witter, IEEE Trans. Magn. **5**, 1099 (1984).
[10] P. Hansen, W. Tolksdorf, and K. Witter, Phys. Rev. B **12**, 2777 (1975).
[11] G. F. Dionne and G. A. Allen, J. Appl. Phys. **73**, 6127 (1993).
[12] G. A. Allen and G. F. Dionne, J. Appl. Phys. **73**, 6130 (1993).
[13] G. F. Dionne and G. A. Allen, J. Appl. Phys. **75**, 6372 (1994).
[14] J. Wei, H. Hu, and H. He, Phys. Status Solidi A **168**, 501 (1998).
[15] A. V. Zenkov and A. S. Moskvin, J. Phys: Condens. Matter **14**, 6957 (2002).
[16] G. Winkler, Magnetic Garnets (Vieweg & Sohn, Braunschweig, 1981).
[17] T. Aichele, A. Lorenz, R. Hergt, and P. Goernert, Cryst. Res. Technol. **38**, 275 (2003).
[18] T. Okuda, T. Katayama, H. Kobayashi, N. Kobayashi, K. Satoh, and H. Yamamoto, J. Phys. A **367**, 4944 (1990).
[19] S. Kahl, S. I. Khartsev, A. M. Grishin, K. Kawano, G. Kong, R. A. Chakalov, and J. S. Abell, J. Phys. A **91**, 9556 (2002).
[20] S. Kahl and A. M. Grishin, J. Appl. Phys. **94**, 5688 (2003).
[21] R. Lux, A. Heinrich, S. Leitenmeier, T. Koerner, M. Herbort, and B. Stritzker, B. J. Phys. A **100**, 113511 (2006).
[22] E. J. Nassar, L. R. Avila, P. F. S. Pereira, C. Mello, O. J. de Lima, K. J. Ciuffi, and L. D. Carlos, J. Lumin. **111**, 159 (2005).
[23] A. Heinrich, T. Koerner, J. Simon, W. Mader, M. Knoll, and A. Kalytta, J. Mag. Soc. Jpn. **32**, 130 (2008).
[24] U. Schubert and N. Huesing, Synthesis of Inorganic Materials (second, revised and updated edition) (Wiley, Weinheim, 2004).
[25] D. Basting, Excimer Laser Technology: Laser Sources, Optics, Systems and Applications (Lambda Physik AG, Goettingen, 2001).
[26] D. H. A. Blank, R. P. J. Ijsselsteijn, P. G. Out, H. J. H. Kuiper, J. Flokstra, and H. Rogalla, Mater. Sci. Eng. **13**, 67 (1992).
[27] D. B. Chrisey and G. K. Hubler, Pulsed Laser Deposition of Thin Films (Wiley & Sons, New York, 1994).
[28] A. V. Gusarov and I. Smurov, J. Phys. A **97**, 014307 (2005).
[29] R. Kelly and R. W. Dreyfus, Nucl. Instrum. Methods **32**, 341 (1988).
[30] S. Leitenmeier, Zum Wachstum von magnetooptischen bismutdotierten Seltenerdeisengranatfilmen, Promotionsschrift, Universitaet Augsburg, 2007.urn:nbn:de:bvb:384-opus-6736.
[31] S. Leitenmeier, T. Koerner, J. Griesbauer, M. Herbort, A. Heinrich, and B. Stritzker, J. Cryst. Growth **310**, 5392 (2008).
[32] W. Braun, Applied RHEED: Reflection High-Energy Electron Diffraction During Crystal Growth (Springer, Berlin, 1999).
[33] P. Yeh, Optical Waves in Layered Media (Wiley, New York, 1988).
[34] T. Koerner, A. Heinrich, M. Weckerle, P. Roocks, and B. Stritzker, J. Appl. Phys. **103**, 07B337 (2008).
[35] A. Heinrich, T. Koerner, J. Simon, W. Mader, M. Knoll, A. Kalytta, S. Horn, and B. Stritzker, J. Magn. Soc. Jpn. **32**(2–2), 130–134 (2008).
[36] T. Koerner, Integration Magnetooptisch Aktiver Granate auf Nicht-Granat-Substraten, Promotionsschrift, Universitaet Augsburg, 2008 (urn:nbn:de:bvb:384-opus-14118).
[37] L. Bergmann, C. Schaefer, and H. Niedrig, Bergmann-Schaefer: Lehrbuchder Experimentalphysik: Band III, Optik (Walter de Gruyter, Berlin, 2004).
[38] R. W. Pohl, Optik und Atomphysik (Springer, Berlin, 1958).
[39] G. N. Babini, A. Bellosi, and P. Vincenzini, J. Mater. Sci. **19**, 1029 (1984).
[40] S. Kahl, Dissertation: Bismuth Iron Garnet Films for Magneto-optical Photonic Crystals, IMFF Stockholm, 2004.